Heterometallic Trinuclear Oxo-centered Clusters as Single-Source Precursors for Synthesis of Stoichiometric Monodisperse Transition Metal Ferrite Nanocrystals

SCHOLARONE™
Manuscripts

Heterometallic Trinuclear Oxo-centered Clusters as Single-Source Precursors for Synthesis of Stoichiometric Monodisperse Transition Metal Ferrite Nanocrystals

Karla R. Sanchez-Lievanos, Mehrin Tariq, William W. Brennessel, and Kathryn E. Knowles*

Department of Chemistry, University of Rochester, Rochester, NY 14627, United States

*Corresponding author: Email address: kknowles@ur.rochester.edu

ABSTRACT

The use of heterobimetallic metal complexes as molecular single-source precursors is a promising strategy for the targeted synthesis of phase-pure stoichiometric ternary metal oxide nanocrystals. However, the design and synthesis of these precursors is not trivial and can require considerable effort. Using spinel metal ferrite nanocrystals of formula MFe_2O_4 ($M = Fe^{2+}$, Co^{2+}, Ni^{2+}, Cu^{2+}, and Zn^{2+}) as a model system, this paper evaluates the efficacy of the single-source precursor approach by comparing directly nanocrystals synthesized from the solvothermal reaction of heterobimetallic trinuclear oxo-bridged clusters of formula $M^{II}Fe^{III}_2(\mu_3\text{-}O)(\mu_2\text{-}O_2CR)_6(H_2O)_3$, $R = CF_3$ to nanocrystals synthesized from the solvothermal reaction of stoichiometric mixtures of multi-source precursors, such as metal acetate or nitrate salts. For each M explored here, the clusters form phase-pure MFe_2O_4 nanocrystals with significantly narrower size distributions than nanocrystals synthesized from multi-source-precursors. In the case of M = Cu, the multi-source metal salt precursors produce a mixture of CuO and $CuFe_2O_4$. Additionally, changing the electronic nature of the R-group on the bridging carboxylate ligand from electron withdrawing (CF_3) to electron donating (CH_3 or $C(CH_3)_3$) decreases the average diameter of the resulting nanocrystals by a factor of two. The cluster molecules therefore offer superior control over both morphology and composition for transition metal ferrite nanocrystals. We hypothesize that this remarkable performance arises from the presence of pre-formed $M^{2+}\text{-}O\text{-}Fe^{3+}$ moieties in the cluster molecules that enable direct nucleation of MFe_2O_4 and preclude nucleation of binary oxide impurities.

INTRODUCTION

Spinel ferrite nanomaterials with formula MFe_2O_4, where M^{2+} is a first-row transition metal, are in the spotlight of current nanoscience and technology due to their relevant applications in the fields of dye degradation,[1, 2] drug delivery,[3] CO_2 reduction,[4] and photoelectrochemical water splitting.[5-7] The chemical, structural, and magnetic properties of these multifunctional materials are influenced directly by their composition and morphology, both of which can be controlled synthetically.[8] Methods for preparing spinel ferrites include conventional high-temperature (ceramic) methods, in which metal precursors are mixed and milled into powders and then heated to elevated temperatures with transitional grinding,[9, 10] and lower temperature methods that involve decomposition or co-precipitation of metal precursors from a solvent.[11]

Synthesizing metal oxide nanomaterials in a reaction solvent provides the opportunity to use solvent properties, ligand structure, and other chemical design strategies to manipulate precursor reactivity and thereby direct nanocrystal nucleation and growth processes to achieve control over nanoparticle morphology.[12] Although this approach has been very successful for binary oxides,[13-15] ternary oxides, which contain two different metals, present the additional challenge of controlling composition and morphology simultaneously. Avoiding formation of binary oxide side products is critical to achieving an efficient synthesis of phase-pure ternary oxide nanocrystals. An attractive strategy to access ternary oxide phases directly is to use mixed-metal molecular single-source precursors that contain both metals in the desired stoichiometry and oxidation states.[16-25] Although this approach offers potentially the most effective way to control composition homogeneity and crystal phase by having the component elements intimately mixed on the molecular level before the reaction even starts, identifying and synthesizing appropriate single-source precursors still present significant challenges.[25]

Molecular inorganic clusters can be used as convenient single-source precursors for high quality, monodispersed nanocrystals of semiconductor materials.[16, 17] In the case of ternary oxide materials, heterometallic trinuclear oxo-bridged carboxylate clusters have been used as single-source precursors for spherical, cubic, and truncated-octahedral MFe_2O_4 (M=Mn, Co, Ni, Zn) nanoparticles with a size range between 5 to 25 nm.[26-29] These synthetic methods involve decomposition of the cluster molecules *via* conventional heat-up[30] or hot injection[26, 31] techniques in diphenyl ether or benzyl ether under reflux at ambient pressure to form phase-pure nanocrystals

with controlled size and shape. However, these studies have only been performed on clusters that have electron-donating substituents on the bridging carboxylate ligands.

Herein, we present new insights into the synthesis of metal ferrite nanocrystals using a series of mixed-valent heterometallic trinuclear oxo-centered homoleptic clusters of the general formula $M^{II}Fe^{III}_2(\mu_3\text{-}O)(\mu_2\text{-}O_2CR)_6(H_2O)_3$, where R = CF$_3$ and M = Fe, Co, Ni, Cu, Zn, as model single-source precursors for spinel metal ferrites with the general formula MFe$_2$O$_4$. In addition to expanding this particular class of trinuclear cluster molecules to include M = Ni, we compare and contrast the nanocrystal products made from these clusters to those obtained from mixtures of metal acetate and metal nitrate salts under solvothermal reaction conditions. We find that the single-source precursor clusters produce phase-pure isotropic MFe$_2$O$_4$ nanocrystals that are significantly more monodisperse in their diameters than nanocrystals synthesized from multi-source precursors. Furthermore, reactions containing mixtures of copper and iron salts as precursors produce a mixture of CuO and CuFe$_2$O$_4$ nanocrystals whereas the Cu-Fe cluster molecule produces phase-pure CuFe$_2$O$_4$ nanocrystals. Finally, we find that changing the R-group of the carboxylate bridging ligand in the cluster with M = Fe from an electron-withdrawing trifluoromethyl group (CF$_3$) to an electron donating methyl (CH$_3$) or *tert*-butyl (C(CH$_3$)$_3$) group decreases the average diameter of the resulting Fe$_3$O$_4$ nanocrystals from 29.8 nm to 16.4 or 14.3 nm, respectively. These results demonstrate the ability to control the morphology of metal ferrite nanocrystals by tuning the electronic properties of the ligands in single-source cluster-based precursors.

EXPERIMENTAL METHODS
Materials.

Iron(III) nitrate nonahydrate (Fe(NO$_3$)$_3$·9H$_2$O, 98+%), iron(III) chloride hexahydrate (FeCl$_3$·6H$_2$O, 97+%), iron(II) chloride tetrahydrate (FeCl$_2$·4H$_2$O, 98+%), iron acetate(II) (Fe(CO$_2$CH$_3$)$_2$, 95+%), cobalt(II) nitrate hexahydrate (Co(NO$_3$)$_2$·6H$_2$O, 98+%), cobalt(II) acetate tetrahydrate (Co(CH$_3$COO)$_2$·4H$_2$O, 98+%), nickel(II) nitrate hexahydrate (Ni(NO$_3$)$_2$·6H$_2$O, 98+%), nickel(II) acetate tetrahydrate (Ni(CH$_3$COO)$_2$·4H$_2$O, 98%), copper(II) nitrate trihydrate (Cu(NO$_3$)$_2$·3H$_2$O, 98+%), copper(II) acetate monohydrate (Cu(CO$_2$CH$_3$)$_2$·H$_2$O, 98+%), zinc(II) nitrate hexahydrate (Zn(NO$_3$)$_2$·6H$_2$O, 98+%), zinc(II) acetate dihydrate (Zn(CH$_3$COO)$_2$·2H$_2$O, 98+%), trifluoroacetic acid (99%), acetic acid (99.7%), pivalic acid (99%), sodium hydroxide

(98%), oleic acid (90%), oleylamine (70%), and dibenzyl ether (99%) were purchased from Sigma Aldrich and used as received without further purification. *Caution! Trifluoroacetic acid is both volatile and corrosive and should therefore be handled exclusively in a fume hood.*

Synthesis of $M^{II}Fe^{III}_2(\mu_3\text{-}O)(\mu_2\text{-}O_2CCF_3)_6(H_2O)_3$

Heterobimetallic trinuclear oxo-centered clusters were prepared according to an adapted literature procedure.[32] $Fe(NO_3)_3 \cdot 9H_2O$ (34 mmol) and $M(NO_3)_2 \cdot nH_2O$ (17 mmol) (M=Co, Ni, Cu and Zn, n=3 or 6) were dissolved separately in vials containing 5 mL of deionized water. For $Fe^{II}Fe^{III}_2(\mu_3\text{-}O)(\mu_2\text{-}O_2CCF_3)_6(H_2O)_3$, $FeCl_3 \cdot 6H_2O$ (34 mmol) and $FeCl_2 \cdot 4H_2O$ (17 mmol) were dissolved together in a vial containing 10 mL of deionized water. NaOH (12 mmol) was dissolved in 15 mL of water and mixed with trifluoroacetic acid (36 mmol) in a 250 mL round-bottom flask. The metal nitrate or metal chloride salt solutions were subsequently added to the resulting solution of sodium trifluoroacetate and the reaction mixture was heated to 85 °C under ambient atmosphere and left stirring for 20 h until a homogeneous solution formed. After cooling, excess trifluoroacetic acid was distilled off under vacuum. The remaining solid product was dissolved in acetone and separated from sodium nitrate *via* vacuum assisted filtration; the formation of sodium nitrate or sodium chloride provides the driving force for the reaction. The resulting filtrate was dried at 45 °C in a rotary evaporator for at least 1 h, yielding a fine powder, which is used in the nanocrystal synthesis without further workup. The clusters were synthesized on average in good yield (83%). The clusters are stable to air and moisture and soluble in polar organic solvents such as acetonitrile, acetone, and pyridine (see Supporting Information†). Single crystals of these clusters were grown for X-ray diffraction analysis by slow evaporation of a concentrated solution of the product in acetone or water. The clusters were also characterized by Fourier-transform infrared spectroscopy (FTIR) and UV-Vis absorption spectroscopy.

Synthesis of MFe_2O_4 Nanocrystals

$M^{II}Fe^{III}_2(\mu_3\text{-}O)(\mu_2\text{-}O_2CR)_6(H_2O)_3$ (0.025 mmol), oleylamine (2.7 mmol), oleic acid (2.7 mmol), and benzyl ether (10 mL) were added to a 25-mL Teflon insert. The mixture was stirred for 30 minutes under ambient conditions to form a clear brown suspension. Subsequently, the Teflon insert was loaded into a stainless-steel autoclave, sealed, and heated at 230 °C for 24 h. The autoclave was allowed to cool down before it was opened to reveal a black (M^{2+}=Fe), dark-

red-brown (M^{2+}= Co), black gray (M^{2+}= Cu) or yellow-brown (M^{2+}= Ni and Zn) suspension. The suspension was then purified with three cycles of precipitation with ethanol followed by centrifugation. The resulting colorless supernatant was discarded, and the precipitate was dispersed in 10 mL of hexane.

Synthesis of MFe_2O_4 nanocrystals from stoichiometric mixtures of metal acetate and nitrate salts

MFe_2O_4 nanocrystals were synthesized using stoichiometric (2:1) mixtures of FeX_3 (0.017 mmol) and MX_2 (0.008 mmol) (X= OAc and NO_3) dissolved in a mixture of oleylamine (2.7 mmol), oleic acid (2.7 mmol) and 10 mL of benzyl ether. The mixture was stirred for 30 minutes under ambient conditions and then heated to 230 ºC for 24 h in a 25-mL autoclave reactor. The solvothermal reactions revealed precipitates with the same color tones of the metal ferrites synthesized from the clusters. For the case of M^{2+}= Cu, the reactions produced a brown-black precipitate rather than a black-gray precipitate

Characterization Methods.

Single-Crystal X-ray Crystallography. Single-crystal X-ray diffraction data were collected for the $M^{II}Fe^{III}_2(\mu_3\text{-O})(\mu_2\text{-O}_2CR)_6(H_2O)_3$ cluster molecules using a Rigaku XtaLAB Synergy-S Dualflex diffractometer equipped with a HyPix-6000HE HPC area detector for data collection at 100.00(10) K (**2**, **3**, **4** and **5**) and at 99.97(10) K (**1**) . The full data collection was carried out using a PhotonJet (Cu) X-ray source with frame times given in the Supporting Information. Structures were solved using ShelXT[33] and refined using ShelXL.[34] Structure manipulation and figure generation were performed using Olex2.[35] Crystal data and refinement parameters are given in Table S1 in the Supporting Information.

Powder X-ray diffraction. The use of a copper source for powder X-ray diffraction analysis of iron-containing samples yields a high background signal due to X-ray fluorescence from iron. Monochromators can be used to suppress this background fluorescence signal; however, this approach presents disadvantages, such as low penetration depth and loss of peak intensity, that can lead to diffractograms with inconclusive peak patterns. Employing molybdenum radiation can help overcome these drawbacks. The lower fluorescence background signal observed using this radiation provides an improved signal to noise ratio and enables unambiguous phase

identification.[36] We therefore performed powder X-ray diffraction measurements using a Rigaku XtaLAB Dualflex Synergy-S diffraction system with MoKα radiation (λ = 0.71073 Å). We converted the 2θ values obtained using the Mo source to 2θ values corresponding to the wavelength of a CuKα source (λ=1.54148 Å) in order to compare our measured spectra to standard data deposited in the JCPDS database that was collected with CuKα radiation (see Supporting Information†). Samples for powder X-ray diffraction measurements were prepared by dropcasting hexane dispersions of purified nanocrystals onto glass substrates under ambient atmosphere. Prior to film fabrication, the glass substrates were cleaned with isopropanol under sonication for 30 minutes.

Transmission Electron Microscopy (TEM). TEM images were taken using a FEI Tecnai F20 TEM with a beam energy of 200 kV. The nanocrystal samples were dropcast onto lacey carbon copper grids from dispersions in hexane. The diameter of the particles was measured using ImageJ software.

X-ray photoelectron spectroscopy (XPS). X-ray photoelectron spectra (XPS) were obtained on a Kratos AXIS Ultra DLD spectrophotometer. Scans were collected using an aluminum anode source with an emission current of 10 mA, an accelerating voltage of 15 kV, and a pass energy of 80 eV. Typical collection times were 10 minutes for the survey scans and 8 minutes for each of the detail scans. All measurements were taken at a pressure $< 5 \times 10^{-7}$ Torr. The beam energy and emission current of the electron gun were 5 eV and 7 μA, respectively. The peak positions for the samples were referenced to the carbon 1s line (284.8 eV). XPS samples were prepared by dropcasting dilute solutions of nanocrystals onto cleaned Si wafers and grounded to the instrument using carbon tape. The ratio between iron and the divalent cation was determined from the ratio of the areas of the Fe 2p and M 2p peaks following a background correction using Tougaard's method in Casa XPS software.

Energy Dispersive X-Ray Spectroscopy (EDS). Energy dispersive X-ray spectroscopy elemental maps were obtained using a Zeiss Auriga Scanning Electron Microscope with an EDS analyzer and EDAX Apex software. Measurements were carried out using 25 kV electron beam.

Absorption Spectroscopy. Absorption spectra of colloidal dispersions of nanocrystals were collected using an Agilent Cary 7000 UV–Vis spectrometer.

RESULTS

Structural Characterization of Heterobimetallic Cluster Molecules

Scheme 1a depicts the synthetic route used to prepare $M^{II}Fe^{III}_2(\mu_3\text{-}O)(\mu_2\text{-}O_2CR)_6(H_2O)_3$ (M = Fe (**1**), Co (**2**), Ni (**3**), Cu (**4**), Zn (**5**)) by reacting commercial $Fe(NO_3)_3\cdot 9H_2O$, $M(NO)_3\cdot nH_2O$, trifluoroacetic acid (TFA) and sodium hydroxide at 85 °C for 20 h. The resulting air-stable powder was further purified with acetone to remove the formed sodium salt. The crystal structures of each of the synthesized clusters **1-5** were obtained through single-crystal x-ray diffraction (see Supporting Information†).
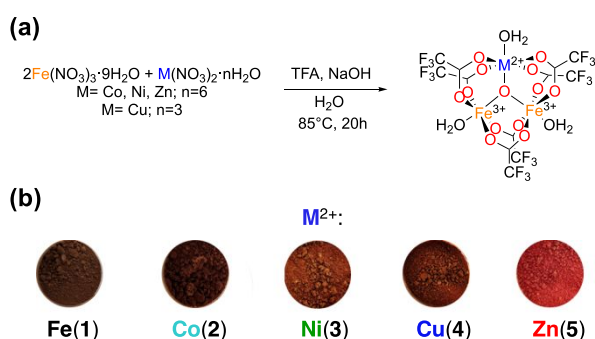
Scheme 1. (a) Reaction scheme for the synthesis of the mixed-valent mixed-metal trimeric oxo-centered clusters **1-5**. **(b)** The images inside the circles under the reaction scheme show the colors of the inorganic cluster powders.

The μ_3-oxo-heterotrinuclear compounds **2**, **4**, and **5** are isostructural with the mixed-valent iron trifluoroacetate complex **1**. These clusters crystallize in the monoclinic space group $C2/c$. Cluster **3** crystallizes isotopically in the triclinic space group $P\text{-}1$. The molecular structure of each mixed-valent cluster contains a triangular arrangement of metal ions, with a μ_3-bridged oxygen atom at the center of the triangle (Fig. 1). The triangular scaffold has different lengths of each edge linking the metal centers, in agreement with the lowering of its symmetry from the ideal C_3 local symmetry of trinuclear trivalent carboxylated clusters.[37] The terminal coordination site of the octahedral metal ions located *trans* to the central oxygen atom is occupied by H_2O. Each pair of metal centers is connected by two bridging bidentate trifluoroacetate ligands. All three metal atom sites in **2**, **3**, and **4** were refined with a mixed occupancy by M and Fe, with a constraint to give a total of 1M:2Fe atoms; on each site a single set of positional and anisotropic displacement parameters were

used. (For **5**, only two metal sites were refined as a mixture of M and Fe; see Supporting Information†).
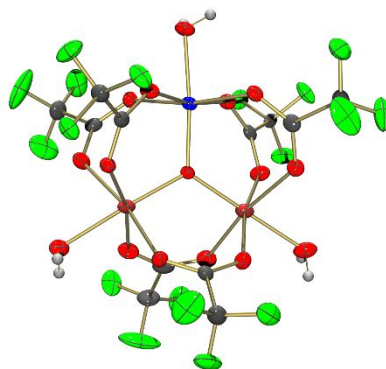

Figure 1. Representative molecular structure of the single-source precursors shown with 50% probability ellipsoids. Color code: white – hydrogen, gray – carbon, red – oxygen, green – fluorine, orange – Fe^{3+} and blue – M^{2+}.

The electronic absorption spectra of the clusters (Fig. 2) are similar to those reported in the literature for trinuclear carboxylates containing iron(III).[38,39] The intense absorption bands centered near 345 and 455 nm correspond to spin-allowed ligand-to-metal charge-transfer (LMCT) transitions characteristic of iron(III) containing systems. Ligand field transitions related to iron(III) and the divalent metal centers are significantly weaker in intensity ($\varepsilon < 100$ $M^{-1}cm^{-1}$) due to the fact that they are forbidden by the Laporte rule.[40] These transitions are highlighted in the inset to Figure 2. Table S3 in the supporting information tabulates the positions and extinction coefficients of these absorption bands.

The IR spectra of clusters **1-5** (see Fig. S3 and Table S4) confirm their purity as well as the bridging bidentate configuration of the OCO^- group by which the trifluorocarboxylate ligands are coordinated to the metal ions.[41]
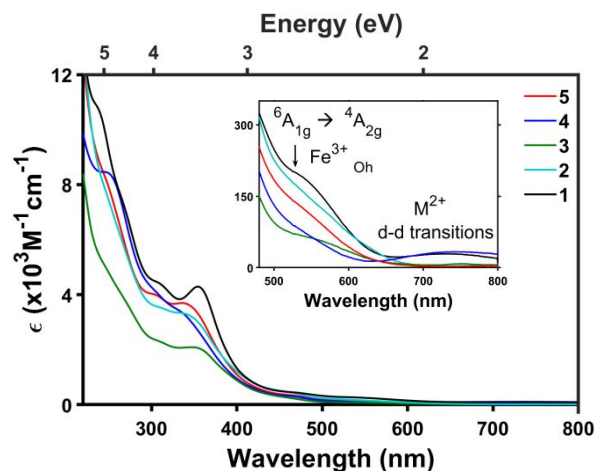
Figure 2. Absorption spectra of the trinuclear clusters **1-5** in acetonitrile solution.

Structural and Spectroscopic Characterization of Ferrite Nanoparticles.

Figure 3 contains representative TEM images of the MFe_2O_4 (M = Fe, Co, Ni, Cu, Zn), nanoparticles obtained from the solvothermal reaction of the corresponding single-source cluster precursors **1-5** (a), and of stoichiometric mixtures of iron and metal acetate (b) and nitrate (c) salts. Superimposed on each image is a plot of a histogram summarizing the distribution of nanocrystal diameters found in that particular sample. These particle-size distributions can be parameterized as polydispersity index (PDI), which is defined in Equation 1 to be the ratio of the standard deviation of the nanocrystal diameter (σ_d) and the average diameter ($\langle d \rangle$).

$$PDI = \frac{\sigma_d}{\langle d \rangle} \tag{1}$$

Nanocrystal samples with a PDI < 0.1 are considered to be monodisperse, those with a PDI between 0.1 and 0.2 are referred to as highly uniform, and a sample with a PDI > 0.2 is considered to be polydisperse.[42] The oxo-centered clusters **1-5** form isotropic nanoparticles with PDI values ranging from 0.06 to 0.13 and average diameters ranging from 7.9 to 29.8 nm (Table 1). Each of these reactions was performed in triplicate and both the average diameters and PDI values were reproducible across all of the trials (see Supporting Information†). We hypothesize that the remarkable monodispersity of MFe_2O_4 nanocrystals synthesized from these clusters is due to their Fe^{3+}-O-M^{2+} bonds, which force the M^{2+} and Fe^{3+} centers to remain in close proximity with the correct stoichiometric ratio until hydrolysis of the cluster precursor triggers nucleation. This "well-mixed" configuration minimizes the roles diffusion and mixing of two different species play in the

nucleation of the ternary metal oxide phase.[25, 43, 44] We suspect that the consequently simpler nucleation pathway enables nucleation to occur over a narrower temperature and/or time interval. Rapid nucleation is crucial to the formation of nanocrystal samples with narrow size distributions.[45] These results improve upon previous reports using heterometallic trinuclear oxo-centered clusters bridged by acetate ($R = CH_3$) and pivalate ($R = C(CH_3)_3$) ligands as single-source precursors for MFe_2O_4 nanocrystals synthesized via rapid injection into hot solvent at ambient pressure. These "hot injection" methods produce nanocrystals with diameters of 9 ± 2 nm (PDI:0.22, Fe_3O_4), 13 ± 4 nm (PDI:0.30, $CoFe_2O_4$), 15 ± 5 nm (PDI:0.33, $ZnFe_2O_4$),[29] and 3.6 ± 0.2 nm (PDI:0.05, $CoFe_2O_4$).[26] The latter results by Abdulwahab, et al. are consistent with our observation of small PDIs from reactions using oleic acid, oleylamine and benzyl ether.

In contrast, using stoichiometric mixtures of multi-source nitrate or acetate salt precursors under the same solvothermal conditions produces nanocrystals with much wider size distributions and larger PDI values (Table 1). Figures 3b and 3c contain representative TEM images and size histograms for MFe_2O_4 (M = Fe, Co, Ni, Cu, Zn) nanocrystals obtained from reactions of 2:1 mixtures of $Fe(OAc)_3:M(OAc)_2$ and $Fe(NO_3)_3:M(NO_3)_2$, respectively. We note that the $CoFe_2O_4$ and $ZnFe_2O_4$ samples synthesized from mixtures of the acetate salts exhibit distinctly bimodal size distributions corresponding to two distinct sub-populations within the same nanocrystal sample.
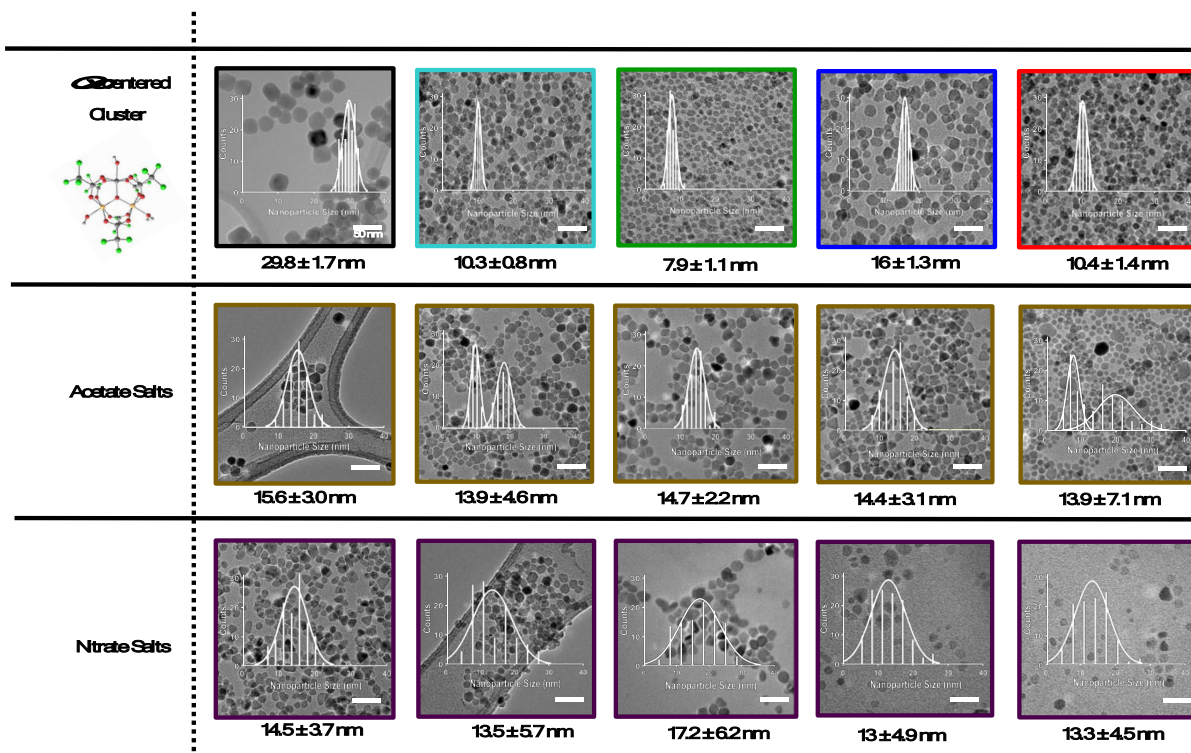
Figure 3. Representative transmission electron micrographs that compare nanocrystals obtained from mixed-metal cluster precursors **1-5** (a) to those obtained from mixtures of metal acetate (b) and nitrate (c) salts. Plots of nanocrystal size histograms are superimposed on the TEM images in white. Each histogram compiles measurements of the sizes of at least 100 nanocrystals. The scale bars represent 50 nm. †$M^{2+}O$ observed on powder XRD diffractogram.

Table 1. Statistical Analysis of the Sizes of MFe_2O_4 Nanocrystals Synthesized from Clusters **1-5**

Metal Ferrite	Cluster Precursor[a]	Acetate Salts[a]	Nitrate Salts[a]
Fe_3O_4	29.8 ± 1.7 (0.06)	15.6 ± 3.0 (0.19)	14.5 ± 3.7 (0.25)
$CoFe_2O_4$	10.3 ± 0.8 (0.07)	13.9 ± 4.6 (0.33)[b]	13.5 ±5.7 (0.42)
$NiFe_2O_4$	7.9 ± 1.1 (0.14)	14.7 ± 2.2 (0.15)	17.2 ± 6.2 (0.36)
$CuFe_2O_4$	16 ± 1.3 (0.08)	14.4 ± 3.1 (0.21)[c]	13.0 ± 4.9 (0.37)[c]
$ZnFe_2O_4$	10.4 ± 1.4 (0.13)	13.9 ± 7.1 (0.51)[b]	13.3 ± 4.5 (0.34)

[a]Average size and standard deviations reported in units of nanometers followed by the PDI in parentheses. [b]Bimodal size distributions observed in histogram. Reported average and standard deviation represent the entire sample. [c]CuO observed by powder X-ray diffraction.

Figure 4 contains powder X-ray diffraction spectra of the five metal ferrite nanocrystal samples obtained from the solvothermal reaction of clusters **1-5** (top) and from solvothermal reactions of mixtures of acetate (middle) and nitrate (bottom) salts. All of these samples exhibit the characteristic cubic spinel diffraction pattern corresponding to the Fd3m space group. Overall, the observed patterns are indexed in good agreement to the standard files obtained from JCPDS (see Fig. S9†). Although each metal ferrite exhibits the same diffraction pattern, they have slightly different lattice parameters. Hence, the positions of the diffraction peaks are slightly different for each M. Figure S10 plots the position of the peak corresponding to diffraction off the {311} plane versus the identity of the metal M in each MFe_2O_4 material. As the atomic number of M increases, the value of 2θ corresponding to the {311} peak increases then decreases. This behavior is consistent with the data obtained from single crystal structures for MFe_2O_4.[45-50] and indicates that we have indeed synthesized each distinct MFe_2O_4 material. Importantly, the diffractograms obtained for nanocrystals synthesized from cluster precursors do not contain any extra diffraction peaks corresponding to impurity phases. In contrast, the diffraction patterns obtained for $CuFe_2O_4$ synthesized from mixtures of copper and iron acetate or nitrate salts contain intense peaks corresponding to CuO phase-impurities.
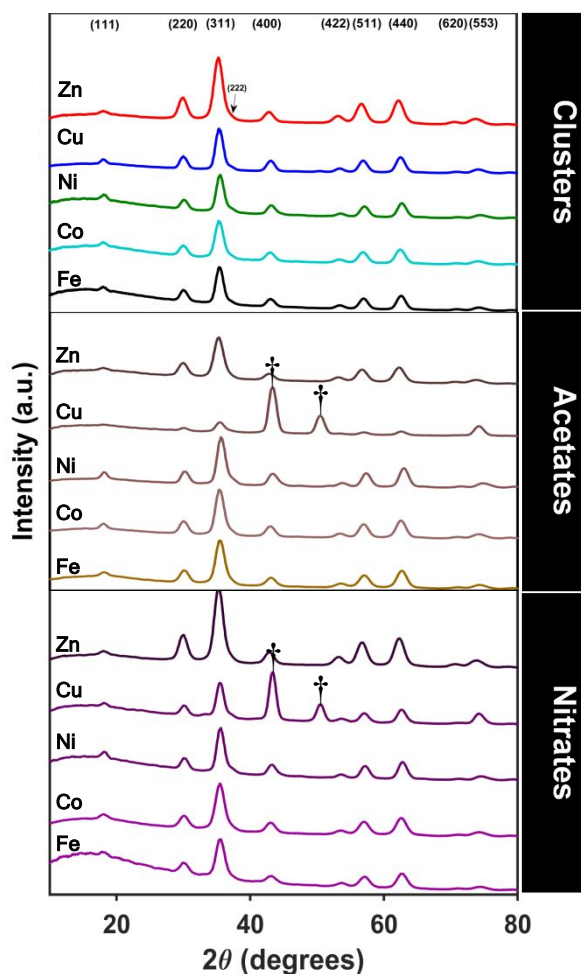
Figure 4. Powder X-ray diffraction spectra of MFe_2O_4 nanocrystals synthesized from the cluster precursors. The representative Bragg planes (111), (220), (311), (222), (400), (422), (511), (440) and (533) peak positions (2θ) agree with their respective JCPDS references (see Supporting Information†).

X-ray photoelectron spectroscopy (XPS) enables us to both confirm the presence of metal ions in their expected oxidation states and quantify their relative surface concentrations within each nanocrystal sample. Table 3 summarizes XPS data obtained for the Fe 2p and M 2p regions for MFe_2O_4 nanocrystals synthesized from the cluster precursors **1-5**. The Supporting Information contains plots of the XPS data (Fig. S11 and Fig. S12†). For M=Fe, the peak positions for Fe $2p_{3/2}$ and Fe $2p_{1/2}$ are 710.4 eV and 724.4 eV, respectively, which are consistent with literature values (see Fig. S12a†).[51] The Fe $2p_{3/2}$ peak can be deconvoluted into two different peaks (709.8 eV and 711.2 eV), showing the two different oxidation states of iron in the sample (Fe^{2+} and Fe^{3+},

1

respectively). However, for M=Co, Ni, Cu and Zn there is only one component in the $2p_{3/2}$ region, which indicates that these metals are present in a single oxidation state in these nanocrystals. The positions of the $2p_{3/2}$ peaks for each of these metals are in good agreement with literature values for their 2+ oxidation states.[52-55] Furthermore, the Co, Ni, and Cu spectra each contain shakeup satellite peaks characteristic of an open-shell electronic configuration. Each of the MFe_2O_4 (M = Co, Ni, Cu, Zn) samples also contains Fe $2p_{3/2}$ peaks centered at 711-712 eV (see Fig. S12f†). Comparing the integrated area of the Fe 2p region to the integrated area of the M 2p region produces an Fe:M ratio close to 2:1 for every sample except the $CuFe_2O_4$ sample, which has a Fe:Cu ratio of 2.5:1. However, the analysis of nanocrystal composition *via* energy dispersive X-ray spectroscopy (EDS) is consistent with a 2:1 Fe:M ratio for all of the samples, including $CuFe_2O_4$ (see Table S8, Table S9 and Fig. S13†). The discrepancy between the XPS and EDS data may arise from differences in the relative *depth of analysis* of the two techniques.[56,57]

Table 3. Binding energies and Fe:M ratios obtained from XPS and EDS measurements of MFe_2O_4 nanocrystals.

Metal Ferrite	Fe $2p_{3/2}$ (eV)	M $2p_{3/2}$ (eV)	Fe:M Ratio	EDS Fe:M Ratio
Fe_3O_4	711.2	709.8	2.01	-
$CoFe_2O_4$	711.0	780.1	2.07	2.03
$NiFe_2O_4$	711.8	855.9	1.98	2.02
$CuFe_2O_4$	712.4	933.2	2.45	2.02
$ZnFe_2O_4$	711.6	1021.5	1.82	2.02

Figure 5 contains ground-state absorption spectra for the MFe_2O_4 nanocrystals synthesized from the cluster molecules **1-5** as well as photographs of the corresponding dispersions in hexane. Each sample exhibits broad absorption across the visible and UV portions of the spectrum with an absorption onset around 1.6 eV (indicated by the vertical dotted line). This onset energy coincides with previously reported diffuse reflectance spectra of nanostructured MFe_2O_4.[57-62] Apart from $NiFe_2O_4$, each spectrum in Figure 5 also contains a broad feature with a peak centered below 1 eV, however, the relative intensity of this feature varies from sample to sample. These variations, along with variations in the shape of the spectrum at energies above the 1.6-eV onset account for the differences in the colors of the dispersions shown in the inset photographs. For Fe_3O_4, the feature

at ~1 eV is assigned to an intervalent charge transfer (IVCT) transition between Fe^{2+} and Fe^{3+} ions in octahedral sites ($^6A_1 \rightarrow {}^4T_1(G)$).[64] The concentration of iron cations in octahedrally coordinated sites impacts the absorption cross-section of this band. As the number of Fe^{2+} and Fe^{3+} ions within the octahedral sites decreases, the intensity of this intervalent charge transfer band also decreases.[65]. Since Fe_3O_4 has the highest concentration of Fe^{3+} and Fe^{2+} ions in octahedral sites, it has a more intense feature at 1eV than any of the other MFe_2O_4 samples. We suspect that the presence of this feature in other MFe_2O_4 samples may indicate the presence of a small concentration of octahedral Fe^{2+}, however, further investigation is required to enable a definitive assignment of this feature.[66]

The assignment of the IVCT feature implies that Fe_3O_4 exhibits the inverse spinel structure in which M^{2+} ions occupy octahedral sites. This structure is expected for Fe_3O_4 because the small crystal field of O^{2-} leads to a high-spin electronic configuration for Fe^{2+}, which prefers octahedral coordination over tetrahedral coordination due to the increased crystal field stabilization energy provided by the octahedral geometry. Since high-spin Co^{2+}, Ni^{2+} and Cu^{2+} also prefer octahedral coordination, we expect $CoFe_2O_4$, $NiFe_2O_4$, and $CuFe_2O_4$ to also adopt an inverse spinel structure. In contrast, Zn^{2+} exhibits no net crystal field stabilization in either an octahedral or tetrahedral geometry, and we therefore expect $ZnFe_2O_4$ to exhibit a mixed spinel structure in which Zn^{2+} and Fe^{3+} each occupy both tetrahedral and octahedral sites. We note that it can be very difficult to distinguish definitively between inverse and normal spinel structures. Single crystal structures reported previously for $CoFe_2O_4$, $NiFe_2O_4$, and $ZnFe_2O_4$ assign at least some degree of mixed occupancy of tetrahedral and octahedral sites,[46, 47, 49] whereas the single crystal data obtained for $CuFe_2O_4$ indicates the inverse spinel structure.[49]
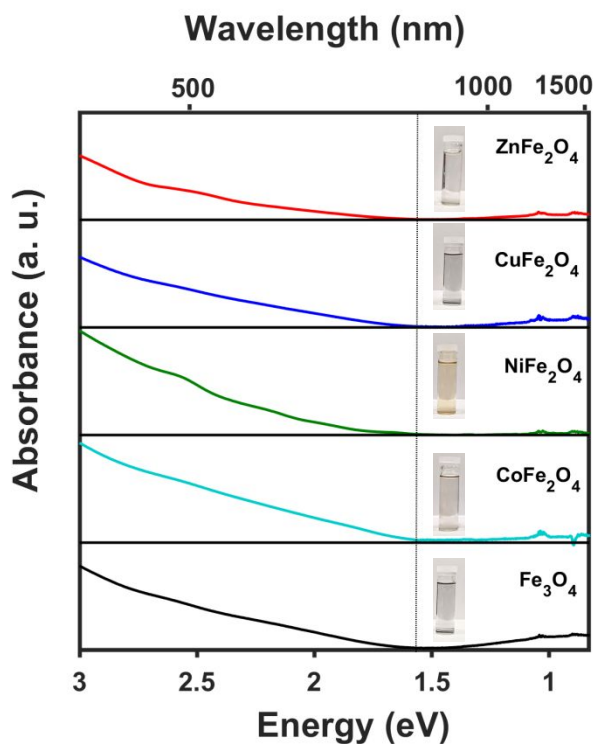
Figure 5. UV-Vis absorption spectra of hexane dispersions of MFe_2O_4 nanocrystals synthesized from clusters **1-5**. The insets depict photographs of the sample dispersions used to obtain each spectrum. The vertical dotted line indicates the absorption onset at ~1.6 eV (~775 nm).

One advantage of using single-source molecular precursors to make metal oxide nanocrystals is the potential to control the reactivity of the precursor by tuning the chemical properties of its ligands. To that end, we synthesized three versions of the mixed-valent iron cluster **1**, each with a different R group on the bridging carboxylate ligands. The R groups we used are $R = CF_3$ (**1**), CH_3 (**1a**), and $C(CH_3)_3$ (**1b**). These R groups differ in their electronic properties (CF_3 is electron-withdrawing and CH_3 and $C(CH_3)_3$ are electron-donating) and steric bulk ($C(CH_3)_3 > CF_3 > CH_3$). Upon solvothermal reaction in benzyl ether in the presence of oleylamine and oleic acid at 230 ºC for 24 h, each cluster (**1**, **1a**, and **1b**) forms phase-pure Fe_3O_4 nanocrystals as confirmed by powder X-ray diffraction data shown in Figure 6c. However, the TEM images shown in Figure 6b demonstrate that the different R groups lead to different nanocrystal sizes. Cluster **1** produces isotropic nanocrystals with an average diameter of 29.8 ± 1.7 nm whereas clusters **1a** and **1b** produce isotropic nanocrystals with diameters of 16.4 ± 1.2 nm and 14.3 ± 0.7 nm, respectively.

The Supporting Information contains data demonstrating the reproducibility of these results. These observations indicate that the electronic properties of the R group have a bigger impact on nanocrystal formation than steric bulk.
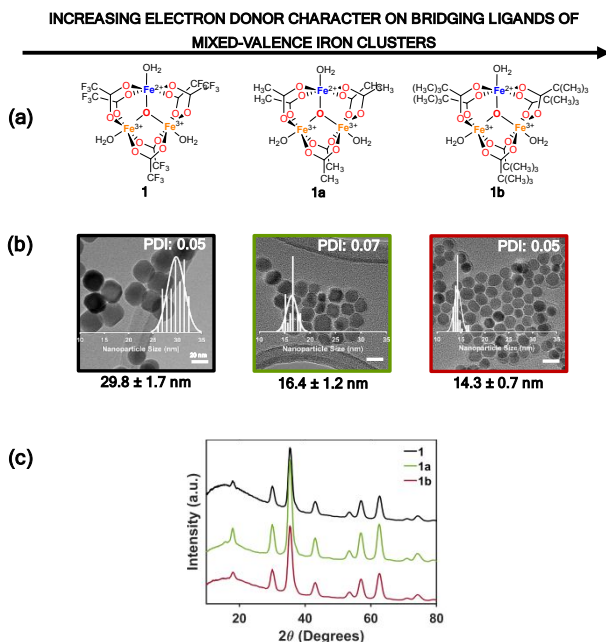

Figure 6. (**a**) Structures of mixed-valent trinuclear oxo-bridged iron clusters $Fe^{II}Fe^{III}_2(\mu_3\text{-}O)(\mu_2\text{-}O_2CR)_6(H_2O)_3$, with R = CF_3 (**1**), CH_3 (**1a**) and $C(CH_3)_3$ (**1b**). (**b**) Representative TEM images of Fe_3O_4 nanocrystals synthesized from clusters **1**, **1a**, and **1b**. Plots of histograms representing the size distribution of each nanocrystal sample are superimposed on each TEM image. The average diameters of these samples are 29.8 ± 1.7 nm (**1**), 16.4 ± 1.2 nm (**1a**), and 14.3 ± 0.7 nm (**1b**). (**c**) Powder X-ray diffraction patterns of nanocrystals obtained from solvothermal reactions of clusters **1**, **1a**, and **1b** are consistent with phase-pure Fe_3O_4.

DISCUSSION

The results presented in the previous section describe two primary observations about the solvothermal synthesis of transition metal ferrite (MFe_2O_4) nanocrystals: (i) using heterobimetallic clusters **1-5** as molecular single-source precursors produces nanocrystals with smaller polydispersity indices (and greater phase purity in the case of M = Cu) than nanocrystals synthesized using mixtures of acetate or nitrate salts, and (ii) changing the electronic character of the R-group on the bridging carboxylate ligands in cluster **1** from electron withdrawing to electron donating produces Fe_3O_4 nanocrystals with a smaller average diameter. Based on these

observations, and on previously proposed mechanisms for solvothermal synthesis of metal oxide nanocrystals,[67] we propose the following mechanism for formation of metal ferrite nanocrystals from single-source cluster molecules **1-5** (Scheme 2a). First, nucleophilic attack of a bridging carboxylate ligand by oleylamine produces an amide and a hydroxylated cluster (steps i-ii). Formation of the amide byproduct proposed here (shown in box) is consistent with observation of peaks corresponding to an amide group in FTIR spectra of supernatants obtained from nanocrystal purification (see Fig. S16†). Any one of the six bridging carboxylates is equally likely to be attacked, therefore, this step could result in hydroxylation of any of the three metal centers in the cluster (iii), or perhaps in the formation of a bridging hydroxide between two of the metal centers. The hydroxylated clusters serve as monomers for nanocrystal formation. We note that, unlike the monomers produced in reactions conducted with mixtures of acetate or nitrate salts, these monomers already contain both M and Fe covalently linked by a bridging oxo ion. Condensation of two hydroxylated cluster molecules initiates nucleation of a MFe_2O_4 nanocrystal (iv). We acknowledge that the proposed mechanism drawn in Scheme 2a implies that the triangular MFe_2O core of the clusters remains intact throughout the precursor conversion and nucleation processes. Although we cannot say with certainty that this is the case, we note that the spinel crystal structure contains a MFe_2O motif that is structurally similar to the MFe_2O core of the cluster precursors (see Supporting Information†).

We observe that cluster **1** is significantly more soluble in the reaction mixture than clusters **1b** and **1c**, and we therefore suspect that monomers derived from **1** are also more soluble than those derived from **1b** or **1c** due to the presence of bridging trifluoroacetate ligands. Increased monomer solubility leads to slower nanocrystal nucleation and ultimately larger nanocrystals.[67, 68] We note that oleic acid may displace one or more of the original bridging carboxylate ligands in the cluster during the initial mixing period before the reaction mixture is loaded into the autoclave. The pKa values of pivalic and acetic acid are similar to the pKa of oleic acid, however, the pKa of trifluoroacetic acid is significantly smaller than that of oleic acid.[69-72] Therefore, oleic acid is much more likely to displace acetate or pivalate from clusters **1a** and **1b**, respectively, than trifluoroacetate from cluster **1**. If this ligand exchange does occur, it does not improve significantly the solubility of the clusters **1a** and **1b** compared to cluster **1**, but it may be responsible for the similarity of nanocrystal sizes obtained from clusters **1a** and **1b**. Ultimately, we attribute the

observed dependence of nanocrystal size on the R-group of the carboxylate ligand to differences in monomer solubility.

Scheme 2b illustrates a proposed mechanism for formation of MFe_2O_4 from mixtures of nitrate or acetate salts. We hypothesize that the first step in these reactions is ligation of the metals by oleic acid (R'-COOH) to form metal oleate complexes. These oleate complexes can then react with the oleylamine to form an amide and a metal hydroxide complex. Condensation of two metal hydroxide complexes initiates nucleation of a metal oxide nanocrystal. Importantly, there are three possible versions of this condensation step: (i) an Fe-OH complex condenses with an M-OH complex to form an Fe-O-M moiety, (ii) two Fe-OH complexes condense to form an Fe-O-Fe moiety, or (iii) two M-OH complexes condense to form an M-O-M moiety. Although the Fe-O-M and Fe-O-Fe motifs formed in possibilities (i) and (ii) appear in the spinel structure of MFe_2O_4, the M-O-M motif formed in possibility (iii) does not. Furthermore, continued self-condensation of either Fe-OH or M-OH monomers could lead to nucleation of binary MO or Fe_2O_3 phases. The relative prevalence of the different condensation reactions (i)-(iii) depends on the relative concentrations of the M-OH and Fe-OH monomers, which in turn depends on the relative rates of the reactions with oleic acid and oleylamine. These variations in the rate of precursor conversion not only lead to formation of MO (as observed in the case of mixtures of Fe and Cu acetate or nitrate) but also lead to broader size distributions.[29, 73]

Figure 7 illustrates the differences between reactions using single-source heterobimetallic molecular precursors compared to multi-source homometallic precursors. We note that oleic acid and oleylamine were present in the same concentrations in the reactions of both the single-source and multi-source precursors. Our previous work demonstrated that the presence of an amine ligand improves the monodispersity of iron oxide nanocrystals synthesized solvothermally.[67] Importantly, because both the single-source and multi-source precursor reactions contained the same concentration of oleic acid and oleylamine, any differences in the polydispersity indices between the two types of reactions can be attributed directly to differences in the type of precursor used.

Finally, the use of a non-aqueous solvent, such as benzyl ether, is crucial for the formation of a spinel ferrite phase. Replacing benzyl ether with water in the solvothermal reaction of the mixed-valent iron cluster **1** produced a vibrant orange-red powder, which is consistent with hematite.[62]

This observation is also consistent with our previous report on the solvothermal synthesis of iron(III) oxide nanocrystals, which demonstrated that the rigorous exclusion of water is necessary for the formation of the spinel magnetite phase. Previous reports also indicate that benzyl ether provides a reducing environment that prevents the oxidation of the divalent ions (M=Fe, Co, Ni).[74]
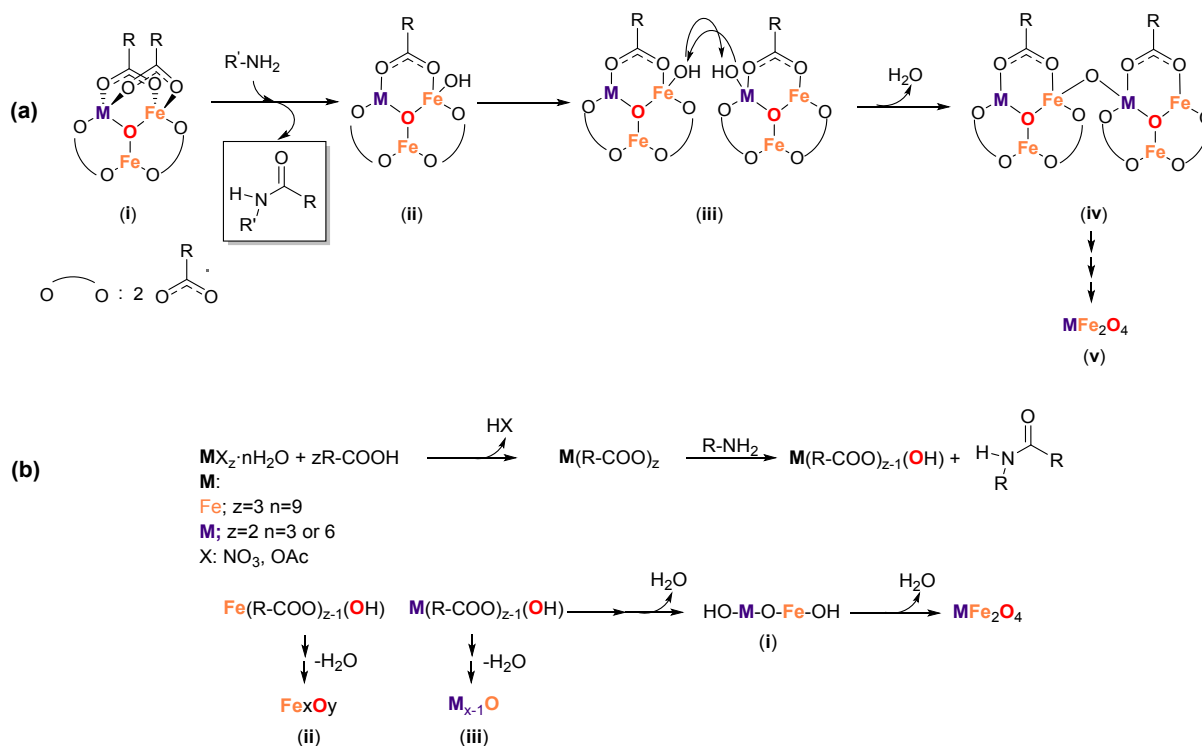
Scheme 2. (a) Proposed mechanism for conversion of single-source precursor clusters **1-5** into metal ferrite nanoparticles. Formation of the amide byproduct proposed here (shown in box) is consistent with observation of peaks corresponding to an amide group in FTIR spectra of supernatants obtained from nanocrystal purification (see Supporting Information†). (b) Mechanism of formation of metal ferrite nanocrystals from mixtures of metal salts. Events (ii) and (iii) open the pathway to generation of binary metal oxides from the hydroxylated monomers.
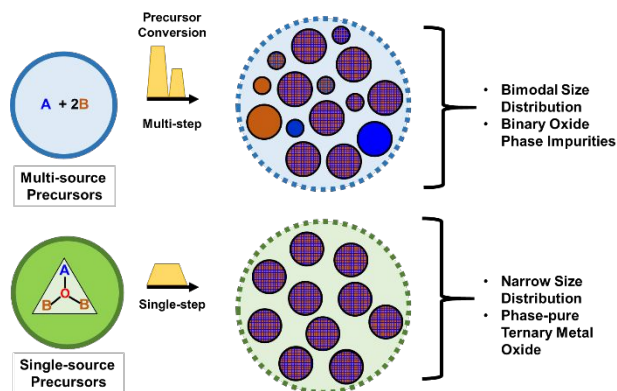
Figure 7. Cartoon comparing the synthesis of metal ferrite nanocrystals from mixtures of metal salts (top) to synthesis using clusters **1-5** as molecular single-source precursors (bottom).

CONCLUSIONS

Using heterometallic trinuclear oxo-bridged clusters **1-5** as molecular single-source precursors in the solvothermal synthesis of metal ferrite nanocrystals MFe_2O_4 (M = Fe, Co, Ni, Cu, Zn) produces nanocrystals with narrower size distributions, but similar average diameters, compared to those obtained from the solvothermal reaction of mixtures of metal acetate or nitrate salts. The cluster precursors also produce phase-pure spinel MFe_2O_4 nanocrystals for each M, whereas for M = Cu, the metal salt precursors form a mixture of $CuFe_2O_4$ and CuO. We attribute the superior performance of the cluster precursors to the fact that they form monomers that contain both M and Fe centers covalently linked via a bridging oxo ion. In contrast, the mixtures of acetate or nitrate salts form separate M and Fe monomers, and hence produce a more heterogeneous nucleation step that leads to larger size distributions and increases the probability of forming binary oxide in addition to ternary oxide phases. We also find that changing the R group on the bridging carboxylate ligands in the mixed-valent iron cluster, **1**, from CF_3 to CH_3 or $C(CH_3)_3$ decreases the average diameter of the resulting Fe_3O_4 nanocrystals by a factor of two. Taken together, these results demonstrate that molecular single-source precursors can enable more precise control over the composition and morphology of ternary oxide nanocrystals.

CONFLICTS OF INTEREST

The authors declare no conflicts of interest.

2

ACKNOWLEDGMENTS

SUPPORTING INFORMATION

The supporting information contains data regarding single-crystal molecular structures, structure refinement, UV-Vis absorption spectra analysis and FT-IR analysis of clusters **1-5**; XRD diffractograms matching JCPDS reference data, X-ray photoelectron survey scan spectra and detail scans for the Fe and M 2p regions, and EDS analysis of the synthesized MFe_2O_4 nanoparticles; UV-Vis absorption and FT-IR transmittance spectrum of **1**, **1a** and **1b**; UV-Vis absorption spectra of hexane dispersions of Fe_3O_4 nanocrystals synthesized from clusters **1**, **1a** and **1b**, representative FT-IR transmittance spectra of the reactants used in the solvothermal reaction *versus* the resulting reaction supernatant; reproducibility test and statistical analysis of the nanoparticles size distribution from different trials of the nanocrystal reactions of **1-5** and **1a**, and **1b**, as well as bulk characterization of clusters **1-5** (FT-IR and EDS).

References

1. N. M. Mahmoodi, *Prog. Color, Color. Coat.*, 2016, **9**, 163 - 171.
2. K. Zaharieva, V. Rives, M. Tsvetkov, Z. Cherkezova-Zheleva, B. Kunev, R. Trujillano, I. Mitov and M. Milanova, *Mater. Chem. Phys.*, 2015, **160**, 271-278.
3. M. Amiri, M. Salavati-Niasari and A. Akbari, *Adv. Colloid Interface Sci.*, 2019, **265**, 29-44.
4. K. M. Rezaul Karim, M. Tarek, H. R. Ong, H. Abdullah, A. Yousuf, C. K. Cheng and M. M. R. Khan, *Ind. Eng. Chem. Res.*, 2019, **58**, 563-572.
5. D. Hong, Y. Yamada, M. Sheehan, S. Shikano, C.-H. Kuo, M. Tian, C.-K. Tsung and S. Fukuzumi, *ACS Sustainable Chem. Eng.*, 2014, **2**, 2588-2594.
6. D. H. Taffa, D. Ralf, A. C. Ulpe, K. C. L. Bauerfeind, B. Thomas, D. W. Bahnemann and M. Wark, *J. Photonics Energy*, 2016, **7**, 012009.
7. R. Dillert, D. H. Taffa, M. Wark, T. Bredow and D. W. Bahnemann, *APL Mater.*, 2015, **3**, 104001.
8. X.-M. Liu, G. Yang and S.-Y. Fu, *Mater. Sci. Eng. C*, 2007, **27**, 750-755.
9. G. Economos, *J. Am. Ceram. Soc.*, 1955, **38**, 241-244.

10.   M. A. Ahmed, E. H. El-Khawas and F. A. Radwan, *J. Mater. Sci.*, 2001, **36**, 5031-5035.
11.   R. T. Olsson, G. Salazar-Alvarez, M. S. Hedenqvist, U. W. Gedde, F. Lindberg and S. J. Savage, *Chem. Mater.*, 2005, **17**, 5109-5118.
12.   R. Deshmukh and M. Niederberger, *Chem. Eur. J.*, 2017, **23**, 8542-8570.
13.   N. Jović Orsini, B. Babić-Stojić, V. Spasojević, M. P. Calatayud, N. Cvjetićanin and G. F. Goya, *J. Magn. Magn. Mater.*, 2018, **449**, 286-296.
14.   M. Tariq, M. D. Koch, J. W. Andrews and K. E. Knowles, *J. Phys. Chem. C*, 2020, **124**, 4810-4819.
15.   H. Chang, B. H. Kim, H. Y. Jeong, J. H. Moon, M. Park, K. Shin, S. I. Chae, J. Lee, T. Kang, B. K. Choi, J. Yang, M. S. Bootharaju, H. Song, S. H. An, K. M. Park, J. Y. Oh, H. Lee, M. S. Kim, J. Park and T. Hyeon, *J. Am. Chem. Soc.*, 2019, **141**, 7037-7045.
16.   N. L. Pickett and P. O'Brien, *Chem. Rec.*, 2001, **1**, 467-479.
17.   M. Veith, *J. Chem. Soc., Dalton Trans*, 2002, DOI: 10.1039/B201383P, 2405-2412.
18.   L. G. Hubert-Pfalzgraf, *J. Mater. Chem.*, 2004, **14**, 3113-3123.
19.   J.-L. Ortiz-Quiñonez, U. Pal and M. S. Villanueva, *ACS Omega*, 2018, **3**, 14986-15001.
20.   C. Panda, P. W. Menezes and M. Driess, *Angew. Chem., Int. Ed. Engl.*, 2018, **57**, 11130-11139.
21.   H. Lu, V. Andrei, K. J. Jenkinson, A. Regoutz, N. Li, C. E. Creissen, A. E. H. Wheatley, H. Hao, E. Reisner, D. S. Wright and S. D. Pike, *Adv. Mater.*, 2018, **30**, e1804033.
22.   J.-P. Jolivet, E. Tronc and C. Chanéac, *C. R. Geosci.*, 2006, **338**, 488-497.
23.   J. A. Garden and S. D. Pike, *Dalton Trans.*, 2018, **47**, 3638-3662.
24.   M. Veith, M. Haas and V. Huch, *Chem. Mater.*, 2005, **17**, 95-101.
25.   H. Lu, D. S. Wright and S. D. Pike, *Chem. Commun.*, 2020, **56**, 854-871.
26.   K. O. Abdulwahab, M. A. Malik, P. O'Brien, G. A. Timco, F. Tuna, C. A. Muryn, R. E. P. Winpenny, R. A. D. Pattrick, V. S. Coker and E. Arenholz, *Chem. Mater.*, 2014, **26**, 999-1013.
27.   M. Moriya, M. Ito, W. Sakamoto and T. Yogo, *Cryst. Growth Des.*, 2009, **9**, 1889-1893.
28.   L. Chen, Y. Shen and J. Bai, *Mater. Lett.*, 2009, **63**, 1099-1101.
29.   K. P. Naidek, F. Bianconi, T. C. R. da Rocha, D. Zanchet, J. A. Bonacin, M. A. Novak, M. das Graças Fialho Vaz and H. Winnischofer, *J. Colloid Interface Sci.*, 2011, **358**, 39-46.
30.   F. J. Douglas, D. A. MacLaren, N. Maclean, I. Andreu, F. J. Kettles, F. Tuna, C. C. Berry, M. Castro and M. Murrie, *RSC Adv.*, 2016, **6**, 74500-74505.
31.   C. P. Guntlin, S. T. Ochsenbein, M. Wörle, R. Erni, K. V. Kravchyk and M. V. Kovalenko, *Chem. Mater.*, 2018, **30**, 1249-1256.
32.   T. Sato, F. Ambe, K. Endo, M. Katada and H. Sano, *J. Radioanal. Nucl. Chem.*, 1995, **190**, 257-261.
33.   G. M. Sheldrick, *Acta Cryst. A*, 2015, **71**, 3-8.
34.   G. M. Sheldrick, *Acta Cryst. C*, 2015, **71**, 3-8.
35.   O. V. Dolomanov, L. J. Bourhis, R. J. Gildea, J. A. K. Howard and H. Puschmann, *J. Appl. Cryst.*, 2009, **42**, 339-341.
36.   Y. M. Mos, A. C. Vermeulen, C. J. N. Buisman and J. Weijma, *Geomicrobiol. J.*, 2018, **35**, 511-517.
37.   T. Y. Glazunova, A. I. Boltalin and S. I. Troyanov, *Mendeleev Commun.*, 2004, **14**, 141-143.
38.   R. D. Cannon and R. P. White, in *Prog. Inorg. Chem.*, 1988, DOI: 10.1002/9780470166376.ch3, pp. 195-298.
39.   J. Šima and J. Makáňová, *Coord. Chem. Rev.*, 1997, **160**, 161-189.
40.   A. B. Blake, A. Yavari, W. E. Hatfield and C. N. Sethulekshmi, *J. Chem. Soc., Dalton Trans.*, 1985, 2509-2520.
41.   S. M. Oh, D. N. Henderickson, K. L. Hassett and R. E. Davis, *J. Am. Chem. Soc.*, 1985, **107**, 8009-8018.
42.   B. Pacakova, S. Kubickova, A. Reznickova, D. Niznansky and J. Vejpravova, *IntechOpen*, 2017, DOI: 10.5772/66074, 1-29.
43.   C. N. R. Rao, *Pure Appl. Chem.*, 1994, **66**, 1765-1772.

44. S. Polarz, A. V. Orlov, M. W. E. van den Berg and M. Driess, *Angew. Chem. Int. Ed.*, 2005, **44**, 7892-7896.
45. L. Qiao and M. T. Swihart, *Adv. Colloid Interface Sci.*, 2017, **244**, 199-266.
46. M. C. Blesa, U. Amador, E. Morán, N. Menéndez, J. D. Tornero and J. Rodríguez-Carvajal, *Solid State Ionics*, 1993, **63**, 429-436.
47. T. A. S. Ferreira, J. C. Waerenborgh, M. H. R. M. Mendonça, M. R. Nunes and F. M. Costa, *Solid State Sci.*, 2003, **5**, 383-392.
48. M. E. Fleet, *J. Solid State Chem.*, 1986, **62**, 75-82.
49. P. F. P. Teh, S. S.; Kim, C.; Chen, C.-M.; Chuang, C.-H.; Sharma, Y.; Cabana, J.; Madhavi, S. , *J. Phys. Chem. C.*, 2013, **117**, 24213-24223.
50. E. J. W. Verwey and E. L. Heilmann, *J. Chem. Phys.*, 1947, **15**, 174-180.
51. T. Yamashita and P. Hayes, *Appl. Surf. Sci.*, 2008, **254**, 2441-2449.
52. Z.-Y. Tian, P. Mountapmbeme Kouotou, A. El Kasmi, P. H. Tchoua Ngamou, K. Kohse-Höinghaus, H. Vieker, A. Beyer and A. Gölzhäuser, *Proc. Combust. Inst.*, 2015, **35**, 2207-2214.
53. P. Li, R. Ma, Y. Zhou, Y. Chen, Q. Liu, G. Peng, Z. Liang and J. Wang, *RSC Adv.*, 2015, **5**, 73834-73841.
54. X. Dong, B. Ren, Z. Sun, C. Li, X. Zhang, M. Kong, S. Zheng and D. D. Dionysiou, *Appl. Catal., B*, 2019, **253**, 206-217.
55. M. Pineda, J. G. Fierro, J. Palacios, C. Cilleruelo, E. García and J. Ibarra, *Appl. Surf. Sci.*, 1997, **119**, 1-10.
56. D. Brabazon and A. Raffer, in *Emerging Nanotechnologies for Manufacturing*, eds. W. Ahmed and M. J. Jackson, William Andrew Publishing, Boston, 2nd edn., 2015, DOI: 10.1016/B978-0-323-28990-0.00003-8, ch. 3, pp. 53-85.
57. S. Tougaard, in *Encyclopedia of Analytical Science* eds. P. Worsfold, C. Poole, A. Townshend and M. Miró, Academic Press, Oxford, 3rd edn., 2013, DOI: 10.1016/B978-0-12-409547-2.00527-8, pp. 400-409.
58. A. Bahadur, A. Saeed, M. Shoaib, S. Iqbal, M. I. Bashir, M. Waqas, M. N. Hussain and N. Abbas, *Mater. Chem. Phys.*, 2017, **198**, 229-235.
59. Muzammil, A. Taufiq, D. Yuliantika, Y. A. Hariyanto, Sunaryono, A. Hidayat, S. Bahtiar, N. Mufti and N. Hidayat, *J. Phys.: Conf. Ser.*, 2018, **1093**, 012020.
60. S.-K. Tong, P.-W. Chi, S.-H. Kung and D.-H. Wei, *Sci. Rep.*, 2018, **8**, 1338.
61. B. S. Holinsworth, D. Mazumdar, H. Sims, Q. C. Sun, M. K. Yurtisigi, S. K. Sarker, A. Gupta, W. H. Butler and J. L. Musfeldt, *Appl. Phys. Lett.*, 2013, **103**, 082406.
62. L. B. Zakiyah, E. Saion, N. M. Al-Hada, E. Gharibshahi, A. Salem, N. Soltani and S. Gene, *Mater. Sci. Semicond. Process*, 2015, **40**, 564-569.
63. M. Sultan and R. Singh, *J. Appl. Phys*, 2009, **105**, 07A512.
64. G. R. Rossman and B. L. Ehlmann, in *Remote Compositional Analysis: Techniques for Understanding Spectroscopy, Mineralogy, and Geochemistry of Planetary Surfaces*, eds. J. F. Bell Iii, J. L. Bishop and J. E. Moersch, Cambridge University Press, Cambridge, 2019, DOI: 10.1017/9781316888872.003, pp. 3-20.
65. U. Hålenius, H. Skogby and G. B. Andreozzi, *Phys. Chem. Miner.*, 2002, **29**, 319-330.
66. H. Liu and C. Di Valentin, *J. Phys. Chem. C*, 2017, **121**, 25736-25742.
67. D. A. Brewster, D. J. Sarappa and K. E. Knowles, *Polyhedron*, 2019, **157**, 54-62.
68. M. P. Hendricks, M. P. Campos, G. T. Cleveland, I. Jen-La Plante and J. S. Owen, *Science*, 2015, **348**, 1226-1230.
69. G. S. Hamilton, in *Encyclopedia of Reagents for Organic Synthesis*, 2001, DOI: 10.1002/047084289X.rp176.
70. J. R. Martin, H. Petitdemange, J. Ballongue and R. Gay, *Biotechnol. Lett.*, 1983, **5**, 89-94.
71. J. R. Kanicky and D. O. Shah, *J. Colloid Interface Sci.*, 2002, **256**, 201-207.
72. M. Namazian, M. Zakery, M. R. Noorbala and M. L. Coote, *Chem. Phys. Lett.*, 2008, **451**, 163-168.

73.   K. M. Ø. Jensen, H. L. Andersen, C. Tyrsted, E. D. Bøjesen, A.-C. Dippel, N. Lock, S. J. L.
        Billinge, B. B. Iversen and M. Christensen, *ACS Nano*, 2014, **8**, 10704-10714.
74.   L. Song, C. Yan, W. Zhang, H. Wu, Z. Jia, M. Ma, J. Xie, N. Gu and Y. Zhang, *J. Nanomater.*,
        2016, **2016**, 1-9

Heterometallic Trinuclear Oxo-centered Clusters as Single-Source Precursors for Synthesis of Stoichiometric Monodisperse Transition Metal Ferrite Nanocrystals

Karla R. Sanchez-Lievanos, Mehrin Tariq, William W. Brennessel, and Kathryn E. Knowles*

Table of Contents Entry
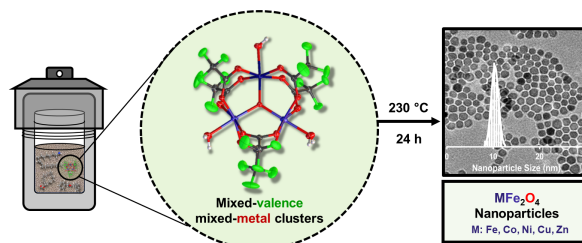
Solvothermal reactions of $M^{II}Fe^{III}_2(\mu^3\text{-}O)(\mu^2\text{-}O_2CR)_6(H_2O)_3$ (R = CF$_3$, M = Fe, Co, Ni, Cu, Zn) clusters produce monodisperse, phase-pure MFe_2O_4 nanocrystals.